Available online at www.sciencedirect.com

ScienceDirect

Thermochimica Acta 461 (2007) 96–106

thermochimica acta

www.elsevier.com/locate/tca

Advanced nonadiabatic ultrafast nanocalorimetry and superheating phenomenon in linear polymers

A.A. Minakov [a,b,*], A.W. van Herwaarden [c], W. Wien [d], A. Wurm [a], C. Schick [a]

[a] *University of Rostock, Institute of Physics, Universitätsplatz 3, 18051 Rostock, Germany*
[b] *A.M. Prokhorov General Physics Institute, Vavilov 38, 119991 Moscow, Russia*
[c] *Xensor Integration, Distributieweg 28, 2645 EJ Delfgauw, the Netherlands*
[d] *DIMES, Delft University of Technology, the Netherlands*

Abstract

To study phase-transition kinetics on submillisecond time scale a set of new membrane gauges for ultrafast scanning nanocalorimetry were constructed. Controlled ultrafast cooling, as well as heating, up to 10^6 K/s was attained. The maximum cooling rate is inversely proportional to the radius of the heated region, which was in the range 10–100 μm for different gauges. The minimum addenda heat capacity was 3 nJ/K. A model describing dynamics of the temperature distribution in the membrane–gas system at ultrafast heating and cooling was developed. The characteristic rate R_0 corresponding to the quasi-static limit of the temperature change in the membrane–gas system was determined. The rate R_0 equals 10^5 K/s for the different gauges in helium gas. The new calorimetric cells in combination with common differential scanning calorimetry (DSC) were applied for the measurements of superheating in a set of linear polymers. A power law relation between the superheating and the heating rate was observed in the broad heating rate range 10^{-2} to 10^5 K/s.

Keywords: Ultra fast scanning calorimetry; Thin-film chip calorimetry; Nanocalorimetry; Superheating

1. Introduction

The nature of melting and crystallization in polymers is a central subject of polymer science [1]. Even for low-molecular systems important details of the solid–liquid transition are still not completely understood [2,3]. A finite latent heat is required to convert the crystal phase to a liquid. Under certain conditions the substance can be overheated or supercooled into a metastable state with respect to equilibrium transition temperature T_0. In order to enlarge the temperature range accessible for the investigation of metastable states, a wide dynamic range for heating and cooling rates is needed.

Polymers can be superheated significantly above T_0 at sufficiently fast heating rate [4–8]. The melting kinetics and superheating in polymers is not understood at present. Generally, at sufficiently low heating rates R, say at $R \sim 1$ K/s, the melting process is accompanied by recrystallization and the shape of melting curves can be very complicated [1,7,9–11]. The first experimental question arises: how to determine the melting temperature $T_m(R)$ in the presence of recrystallization? Recently, it was found that the recrystallization can be avoided for several polymers at heating rates above 10^3 K/s [9–11]. Next, as we have found, the ultrafast rates up to 10^5 K/s are required to measure the critical instability of superheating in polymers. In fact, there is a critical temperature above which a solid cannot be heated without transforming it into a liquid [12–18]. A crystal becomes unstable above this critical superheating and a catastrophic melting process is initiated. To measure the critical superheating in polymers at such heating rates the sample should be thin enough, ∼10 μm, because of heat transfer limitations [19]. Consequently the experimental technique should be quite sensitive for measuring samples in the nanogram range. At last, but not least, the initial sample state must be definite and reproducibly prepared. For example, the sample should be reproducibly quenched from the molten state to a crystallization temperature T_c, then isothermally crystallized at T_c during a definite crystallization time t_c, and heated with a definite rate to the melt. Therefore we need a sample-processing system with possibility to scan temperature $T(t)$ at ultrafast rates with at least millisecond time resolution. The ultrafast *cooling* process should be controlled as well as

---

[*] Corresponding author. Fax: +7 495 135 82 81.
E-mail address: minakov@nsc.gpi.ru (A.A. Minakov).

0040-6031/$ – see front matter © 2007 Elsevier B.V. All rights reserved.
doi:10.1016/j.tca.2007.03.020

heating. For such measurements we have constructed a sensitive ultrafast nonadiabatic calorimeter [19,20].

In the first part of the paper we consider the basic principles of the ultrafast nonadiabatic calorimetry and describe the equipment utilizing a set of new membrane gauges now available from Xensor Integration [21]. Next, as an example, we present the results of superheating of the melting transition for a set of linear polymers. Combining standard differential scanning calorimetry (DSC) and ultrafast nanocalorimetry we have performed measurements in a quite broad range of heating rates 10^{-2} to 10^5 K/s. Calorimeter performance at ultrafast rates and temperature calibration of DSC and ultrafast measurements have been verified by a set of test experiments.

2. Ultrafast nonadiabatic calorimetry

A sensitive and ultrafast calorimeter can be constructed using silicon–nitride membrane technology. Such calorimeter consists of a submicron amorphous silicon–nitride membrane with a thin-film heater and a temperature sensor located at the central part of the membrane. Ultrafast thin-film membrane calorimetry has been advancing rapidly in the recent years [22–26]. Nano- and even pJ/K sensitivity of thin-film calorimeters is primarily related to a very small addenda heat capacity. The ultrafast membrane calorimeters were used for heat capacity measurements of ultra-thin films [22,23] as well as nanoparticles and nanostructures [24,25]. The ultrafast scanning calorimetry provides excellent opportunity to study kinetics of thermodynamic processes on submillisecond time scale and at fast (up to 10^7 K/s [26]) heating rates. While heating rate can be enlarged under quasi-adiabatic conditions by increasing heating power and decreasing sample mass [22–26], the only way to increase the cooling rate is diminishing of addenda and sample heat capacities and performing the experiments at essentially *nonadiabatic* conditions.

To allow fast cooling the measurements can be performed in an ambient gas atmosphere. More over, the maximum rate of controlled cooling can be achieved with a gas cooling agent, rather than in a system with a solid heat-sink, because of the very small thermal inertia of the gas [19,20]. A thin-film membrane calorimeter is quite well adapted for fast cooling experiments, because of very small thermal inertia of the membrane and the ambient gas. Next we consider the optimal conditions for realizing maximum cooling rate. Recently, we have utilized the commercially available microchip (thermal conductivity vacuum gauge, TCG 3880, from Xensor Integration [21], NL) for calorimetry at heating and *cooling* rates up to 10^4 K/s [9–11,19,20]. Since the gauge TCG 3880 initially was not optimized for fast-scanning calorimetry we have developed a set of calorimeter sensors (XEN-3935, XEN-3940, XEN-3969, and XEN-3973 [21]), which allow us to get scanning rates (including cooling) up to 10^6 K/s.

2.1. Measuring cell and upper limit of cooling rate

A cross-sectional view of the calorimeter cell with a sample is schematically shown in Fig. 1. The gauge XEN-3940 shown in Fig. 1 consists of a submicron amorphous silicon–nitride membrane with a thermopile (of six thermocouples) and a resistive heater (~1 kΩ) located at the center of the membrane. The heater strips and all electrical leaders (including thermopile) are formed by p- and n-type polysilicon tracks with specified thermoelectric properties and resistivity. The thermopile hot junctions are arranged in the central part of the heated area between heater stripes. The cold junctions are placed at the silicon frame fixing the membrane at a distance ~1 mm from the center. Thus, the cold-junction temperature equals the temperature of the holder which is close to the temperature of the thermostat T_t. The silicon frame with the membrane is bonded on a standard chip carrier. The whole assembly can be taken out of the thermostat and positioned under a microscope for sample handling. The gauge being installed in a thermostat with controlled temperature and gas pressure can be utilized as a calorimeter for samples in the nanogram range.

To allow fast cooling the cell operates in an ambient gas, which serves as cooling medium providing heat transfer between the sample and the thermostat. Usually, the sample temperature $T(t)$ is scanned linearly with time. In order to derive the optimum conditions for highest cooling rates we consider a saw-tooth shaped heating–cooling process with the scanning temperature range ΔT and the scanning time interval τ. Then the sample temperature is driven by a periodic heat flux $q(t)$ with an amplitude q_0 supplied to the sample–heater interface. Recently, for such scanning process and one-dimensional geometry, we have proved [19] that the product $\Delta T|\mathrm{d}T/\mathrm{d}t|$ cannot exceed $q_0^2/\rho c\lambda$, where ρ, c and λ are the density, the specific heat capacity and the thermal conductivity of the cooling medium, respectively. Provided heat capacity of the sample and addenda are negligibly small, the product $\Delta T|\mathrm{d}T/\mathrm{d}t|$ attains the maximum value $q_0^2/\rho c\lambda$ at any τ in the range $0 < \tau < \tau_0$, where $\tau_0 = \pi\rho c L^2/\lambda$ and L is the distance between the heater and the thermostat. In fact, $\Delta T \sim \sqrt{\tau}$ and $\mathrm{d}T/\mathrm{d}t \sim 1/\sqrt{\tau}$ at $\tau < \tau_0$ and the product $\Delta T|\mathrm{d}T/\mathrm{d}t|$ is invariant with respect to the scanning time interval [19]. The sample temperature is changing around the average value $T_t + T_B$ with the bias temperature $T_B = q_0 L/\lambda$, which should be in the limits required by the experiment. Also the scanning range is restricted to a smallest acceptable $\Delta T_{\min}$. Then, for the maximum rate we have the following relation:

$$\left|\frac{\mathrm{d}T}{\mathrm{d}t}\right|_{\max} \approx \left(\frac{q_0}{\rho c L}\right)\left(\frac{T_B}{\Delta T_{\min}}\right). \qquad (1)$$

Thus, to realize the maximum rate with a reasonably large ΔT the parameter ρc should be reduced as much as possible, i.e. the thermal "inertia" of the cooling medium should be small. We can exemplify this result, say, for $q_0 = 2\times10^5$ W/m^2, $T_B = 300$ K, $\Delta T = 100$ K and $L = \lambda T_B/q_0$. Then, for nitrogen gas with $\lambda_g \approx 2.6\times10^{-2}$ W/K m, $c_g \approx 1.04$ J/g K, $\rho_g \approx 1.19\times10^{-3}$ g/cm^3 at 10^5 Pa [27] and $\rho_g \approx 1.19\times10^{-5}$ g/cm^3 at 10^3 Pa we have $|\mathrm{d}T/\mathrm{d}t|_{\max} \approx 10^7$ K/s and 10^9 K/s, respectively. In contrast, for amorphous silicon–nitride – the material of the membrane – the maximum rate equals ca. 50 K/s at $\lambda_0 \approx 3$ W/K m, $c_0 \approx 0.71$ J/g K and $\rho_0 \approx 3.4$ g/cm^3 [28,29]. Consequently, the cooling medium should be a gas even at a low pressure, as long as the gas

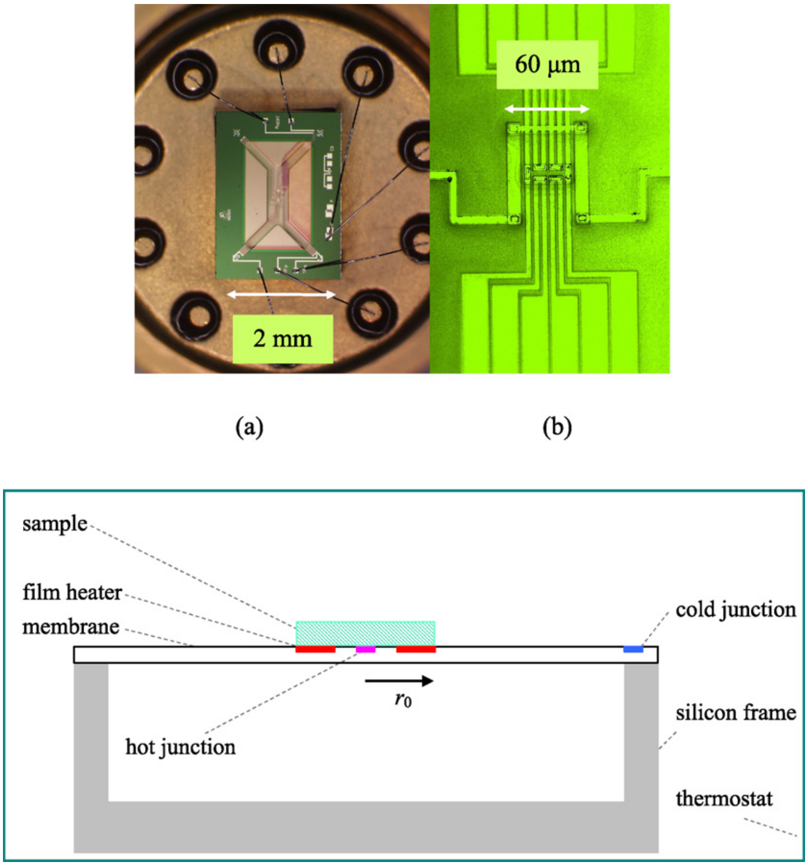

Fig. 1. Photograph of the gauge XEN-3940 utilized as a measuring cell. (a) Rectangular 2 mm × 3 mm silicon frame supporting submicron silicon–nitride membrane is bonded on a standard chip holder. (b) Zoomed photograph of the central part of the membrane with 60 µm × 60 µm heater at the middle and six hot junctions of the thermopile located between two parallel heater stripes. And schematic cross-sectional view of the gauge with the sample is shown at the bottom (not to scale).

thermal conductivity stays reasonably large. In our experiments the heat transfer through the ambient gas is dominant because the membrane is very thin. The measurements are performed in nitrogen gas at reduced pressure $p \sim 10^3$ Pa or in helium gas in the pressure range 10^3–10^4 Pa. Note, the mean free path in the gases – $l_f < 10\ \mu$m at $p > 10^3$ Pa [27] – is still small with respect to the other length parameters.

In fact, the sample heat capacity with addenda is not negligible and the heat-transfer from the heater to the thermostat cannot be considered as a one-dimensional problem. Next, we estimate the maximum cooling rate of the sample for the experimental setup schematically shown in Fig. 1. The central heated region of the membrane can be considered as a small (point-like) source of the heat flow Φ_g into the gas, because of nearly spherical temperature distribution $T_g(r) \approx T_t + (T - T_t)r_0/r$ around the heated region in the gas at the distance from the membrane center $r > r_0$ [20]. Then the heat flow from the sample can be estimated as $\Phi_g \approx -4\pi r^2 \lambda_g \mathrm{d}T_g(r)/\mathrm{d}r$ at $r = r_0$, that is $\Phi_g = (T - T_t)G$, where the heat-transfer coefficient through the gas equals $G \approx 4\pi r_0 \lambda_g$. This approximation was confirmed in [9,10,19,30]. Thus, at room temperature for the gauge XEN-3940 with $r_0 \approx 40\ \mu$m the estimated value G equals about 10^{-5} W/K and 5×10^{-5} W/K in nitrogen and helium gas, respectively, at corresponding thermal conductivities of nitrogen gas 0.026 W/K m and of helium gas 0.152 W/K m [27]. This estimation is confirmed in the experiment. The effect of the membrane on the total heat exchange is relatively small because the membrane is very thin. The heat flow through the membrane in radial direction is at least 10 times smaller than that through the gas in the perpendicular direction [9,10,19,20,30].

If the heat-flow from the heated region into the environment is determined mainly by the heat-transfer through the gas, then the maximum cooling rate for a sample with heat capacity C_s equals

$$\left|\frac{\mathrm{d}T}{\mathrm{d}T}\right|_{\max} = \frac{(T_{\max} - T_t)G}{(C_s + C_A)}, \tag{2}$$

where $T_{\max}$ is the maximum sample temperature and C_A is the addenda heat capacity. Assume the addenda heat capacity can be neglected. Then, for a disk-like sample of thickness d_s and of radius r_0 the maximum cooling rate is $|\mathrm{d}T/\mathrm{d}t|_{\max} \approx 4(T_{\max} - T_t)\lambda_g/r_0 d_s \rho_s c_s$, where ρ_s and c_s are the density and the specific heat capacity of the sample. Consequently, the maximum rate is inversely proportional to the radius r_0. Thus, for $r_0 = 40\ \mu$m at $(T_{\max} - T_t) = 300$ K, $d_s = 5\ \mu$m and $\rho_s c_s = 2 \times 10^6$ J/K m^3, the maximum rate equals $\sim 10^5$ K/s in nitrogen gas and $\sim 5 \times 10^5$ K/s in helium gas. The maximal rate can be even more increased by decreasing of r_0 as long as the radius is large enough with respect to the membrane thickness d_0 and d_s is small enough to neglect the thermal gradient in the sample.

Suppose, the acceptable maximal temperature difference across the sample equals δT_s, then the limitation for heating rate is $\rho_s c_s d_s|\mathrm{d}T/\mathrm{d}t| < \lambda_s\, \delta T_s/d_s$, which is equivalent to the limit for the sample thickness $d_s < (\lambda_s\, \delta T_s/\rho_s c_s|\mathrm{d}T/\mathrm{d}t|)^{1/2}$. Therefore, the thickness d_s should not exceed 1 μm for a polymer sample at $\rho_s c_s = 2 \times 10^6$ J/K m^3, $\lambda_s = 0.3$ W/K m, $\delta T_s = 3$ K and $|\mathrm{d}T/\mathrm{d}t| \sim 10^6$ K/s.

A set of gauges with different dimensions of the heated regions is shown in Fig. 2. The gauge XEN-3973 with the central heated part 18 μm × 20 μm can be used for ultrafast cooling experiments up to 10^6 K/s in helium gas.

To estimate the addenda heat capacity C_A of the gauges consider the temperature distribution $T(x, y)$ in the membrane plane around the heater in Cartesian coordinate system with the origin O at the center of the membrane, axis Oz perpendicular to the membrane, axes Ox and Oy correspondingly parallel and perpendicular to the heater strips. At quasi-static conditions the function $T(x, y)$ is described by the following equation:

$$\frac{\partial^2 T}{\partial x^2} + \frac{\partial^2 T}{\partial y^2} = (T - T_t)\xi_0^2, \tag{3}$$

where $\xi_0^2 = \lambda_g/\lambda_0 d_0 L$ [19,20]. The thermal gradient along Oz axis in a thin membrane placed in a gas is insignificant, provided $\lambda_g(T - T_t)/L \ll \lambda_0\xi_0(T - T_t)$, i.e. $\lambda_g d_0/\lambda_0 L \ll 1$. This is the criterion for a thin membrane. The temperature in the membrane plane exponentially decreases with the distance from the central heating region [19,20]. The characteristic length $1/\xi_0$ of the exponential decay depends on the membrane and the gas thermal conductivity, as well as on the distance from the heater to the thermostat and the membrane thickness. Thus $1/\xi_0$ is about 200 μm for nitrogen gas and 100 μm for helium gas at the thickness $d_0 \sim 1$ μm and the distance from the membrane to the chip holder $L \approx 0.5$ mm. The distance from the central heated region to the membrane periphery is large with respect to the length $1/\xi_0$, i.e. the temperature drops down significantly at membrane periphery. Hence, the boundary conditions at the membrane periphery are not essential for the shape of the temperature distribution near the heater. The result from the analytical solution [19] was confirmed by means of fast infrared thermographic measurements under static and oscillating heating–cooling conditions [20]. Then, the effective radius of the heated region of the membrane can be estimated as a sum $r_0 + \alpha/\xi_0$, where α is a dimensionless parameter of the order of 1. Actually, we obtained from the experiment α equals about 0.2 (see below). Then, the addenda heat capacity can be estimated as $C_A \approx \pi d_0 \rho_0 c_0 (r_0 + \alpha/\xi_0)^2$.

The dynamic heat transfer problem for the membrane placed in a gas is described by the following equation obtained in the same way as Eq. (3) [19,20]:

$$\frac{\partial^2 T}{\partial x^2} + \frac{\partial^2 T}{\partial y^2} = (T - T_t)\xi_0^2 + \left(\frac{1}{D_0}\right)\frac{\partial T}{\partial t}, \tag{4}$$

where the thermal diffusivity of the membrane $D_0 = \lambda_0/\rho_0 c_0$. In case of stationary harmonic temperature oscillations exited by a point source located in the membrane center the solution of Eq. (4) equals $T(x, y, t) = T_t + T_\omega \exp[\mathrm{i}(\omega t - k_x x - k_y y)] \exp(-\xi_x x - \xi_y y)$. The temperature oscillations exponentially decay with the distance from the source at characteristic length $1/\xi$ described by

$$(\xi + \mathrm{i}k)^2 = \xi_0^2 + \frac{\mathrm{i}\omega}{D_0}, \tag{5}$$

where $\xi^2 = \xi_x^2 + \xi_y^2$, $k^2 = k_x^2 + k_y^2$. This is the dispersion law of the thermal waves in the membrane. The complex Eq. (5) is equivalent to the relations $k = \omega/2\xi D_0$ and $\xi^2 = \xi_0{}^2 + (\omega/2D_0\xi)^2$. From the last relation follows

$$\xi(\omega)^2 = \frac{1}{2}\xi_0^2\left(1 + \sqrt{1 + \left(\frac{\omega}{\xi_0^2 D_0}\right)^2}\right). \tag{6}$$

The coefficient $\xi(\omega)$ can be presented as a function of the temperature-modulation rate amplitude $R_\omega = \omega T_\omega$. Then, from Eq. (6) we have $\xi(R_\omega)^2 = (1/2)\xi_0^2(1 + \sqrt{1 + (R_\omega \tau_0/T_\omega)^2})$, where the characteristic time constant of the thermal relaxation in membrane equals

$$\tau_0 = \frac{1}{\xi_0^2 D_0}, \tag{7}$$

also τ_0 can be expressed as follows: $\tau_0 = \rho_0 c_0 d_0 L/\lambda_g$.

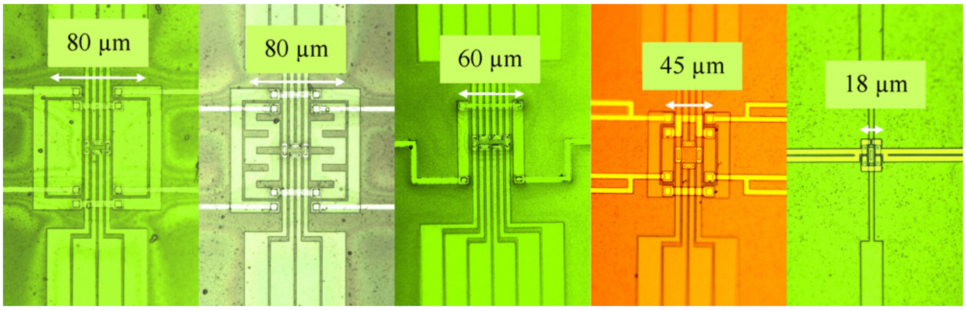

Fig. 2. Photographs (zoomed) of the central part of the membrane for the gauges with different dimensions of the heated regions. From left to right: for XEN-3935, XEN-3936, XEN-3940, XEN-3969, and XEN-3973. The hot junctions of the thermopile are located between two parallel heater stripes. The second outer heaters of the gauges XEN-3935, XEN-3936, and XEN-3969 were not utilized in the present work.

Next, consider a saw-tooth shaped heating–cooling process with the period τ_p, the scanning temperature range ΔT, and the rate $R = 2\Delta T/\tau_p$. This periodic process can be expressed as a sum of harmonic oscillations. The characteristic length $1/\xi(R)$ for this scanning process is of the order of the length $1/\xi(\omega)$ for the main harmonic $\omega = 2\pi/\tau_p$ of the saw-tooth process. In fact, $\xi(R) = (1/\sqrt{2})\xi_0\sqrt{1+\sqrt{1+(R/R_0)^2}}$, where $R_0 = 2\Delta T/\tau_0$. The characteristic rate R_0 corresponds to the maximum rate of the quasi-static temperature change in the membrane. At low rate $\xi(R) \approx \xi_0$ and $\xi(R) \sim \xi_0(R/R_0)^{1/2}$ at $R \gg R_0$. Then, the addenda heat capacity can be expressed as follows:

$$C_A(T, R) = C_0\left(1+\frac{a}{\sqrt{1+\sqrt{1+(R/R_0)^2}}}\right)^2, \qquad (8)$$

where $C_0 = \pi r_0^2 d_0\rho_0 c_0$ and $a = \sqrt{2}\alpha/r_0\xi_0$.

The experimental dependence of C_A versus R for different gauges at 0 °C and 100 °C in helium gas at 6×10^3 Pa are presented in Fig. 3. The measured curves are well described by Eq. (8) at corresponding parameters C_0, a, and R_0. For all gauges we have found $R_0 = (1.3 \pm 0.2) \times 10^5$ K/s in helium gas at $\Delta T = 493$ K in nice agreement with $2\Delta T/\tau_0 = 1.24 \times 10^5$ K/s at $\tau_0 = \rho_0 c_0 d_0 L/\lambda_g$, which equals $\tau_0 = 7.9 \times 10^{-3}$ s for helium gas at $\lambda_g = 0.152$ W/K m. The characteristic rate R_0 measured in nitrogen gas at $\Delta T = 460$ K equals $(1.8 \pm 0.2) \times 10^4$ K/s in agreement with the rate $2\Delta T/\tau_0 = 1.98 \times 10^4$ K/s at $\tau_0 = 4.6 \times 10^{-2}$ s as calculated for nitrogen gas at $\lambda_g = 0.026$ W/K m. The characteristic time constant $2\Delta T/R_0$ determined in helium and nitrogen gas equals $(7.5 \pm 0.5) \times 10^{-3}$ s and $(5.0 \pm 0.3) \times 10^{-2}$ s, respectively. The results are the same at different gas pressure at least in the range $(3–12) \times 10^3$ Pa as shown in Fig. 4. For nitrogen and helium gases at different pressures the parameter C_0 equals 3.0 ± 0.1 nJ/K, 16 ± 0.5 nJ/K, and 21 ± 2 nJ/K for the gauges XEN-3973, XEN-3940, and XEN-3935, respectively, which is comparable to the respective values 3.0, 13.6, and 24.3 nJ/K estimated according to the relation $C_0 = \pi r_0^2 d_0 r_0 c_0$. We assume for the estimation that the radius r_0 equals half of diagonal of the rectangular heated region. Thus, at high rates $R \gg R_0$ the addenda heat capacity tends to its minimum value C_0, which depends only on the size of the heated region.

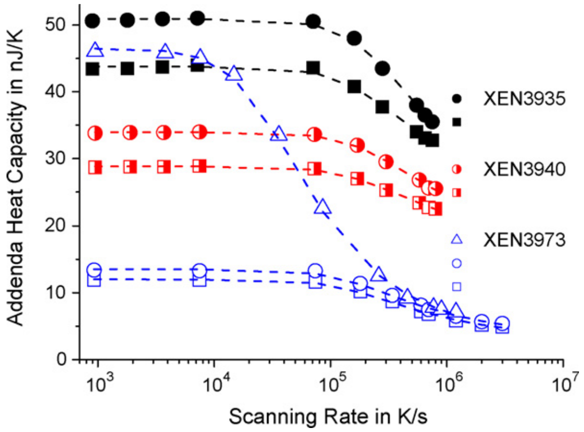

Fig. 3. Scanning rate dependences of the addenda heat capacity C_A for the gauges XEN-3935 (filled symbols), XEN-3940 (half-filled symbols), and XEN-3973 (open symbols) at 0 °C (squares) and 100 °C (circles) in helium gas at 6×10^3 Pa. The same dependence in nitrogen gas at 3×10^3 Pa and 100 °C is shown for the gauge XEN-3973 (triangles). The curves calculated according to Eq. (8) are the dashed lines.

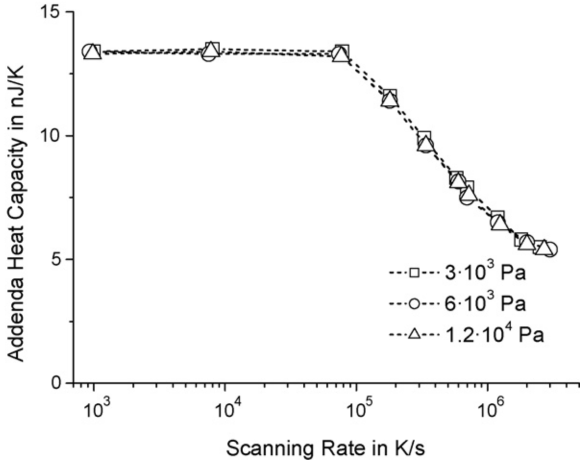

Fig. 4. Scanning rate dependences of the addenda heat capacity C_A for the gauge XEN-3973 at 100 °C in helium gas at pressure 3×10^3 Pa (squares), 6×10^3 Pa (circles), and 1.2×10^4 Pa (triangular).

Below the characteristic rate R_0 the temperature distribution in the membrane is close to the quasi-static distribution calculated and measured in [19,20]. The range of the rates related to the quasi-static scanning is about six times broader in helium gas than in nitrogen gas and it does not depend on the gauge (see Fig. 3). The addenda heat capacity depends on the size of the heated region r_0 and on the gas thermal conductivity as $C_A \sim r_0^2[1+(\alpha/r_0\xi_0)]^2$, where $\xi_0^2 \sim \lambda_g$. Therefore, the addenda heat capacity C_A in helium gas is smaller than in nitrogen gas as shown in Fig. 3 for the gauge XEN-3973. For pressures in the range $(3–12) \times 10^3$ Pa the parameter a of Eq. (8) equals 1.6 ± 0.1 and 4.2 ± 0.2 for the gauge XEN-3973 in helium and nitrogen gas, respectively, which is comparable to the respective values 1.8 and 4.2 estimated at $\alpha = 0.2$.

Next, the heat flow Φ_P in radial direction through the heater perimeter P into the membrane can be estimated as $\Phi_P \approx (T - T_t)\xi(R)\lambda_0 d_0 P$, where the perimeter of the heater $P \approx 2\pi r_0$. The heat flow $\Phi_P(R)$ must be small with respect to the heat flow through the gas $\Phi_g \approx 4\pi(T - T_t)r_0\lambda_g$ in the perpendicular direction. Otherwise the temperature gradient in the radial direction can be significant. Consider the ratio $\Phi_P(R)/\Phi_g$, which equals $\varepsilon \approx (\lambda_0 d_0/4\lambda_g L)^{1/2}$ at $R \ll R_0$ when $\xi(R) \approx \xi_0$, and $\Phi_P/\Phi_g \approx \varepsilon(R/2R_0)^{1/2}$ at $R \gg R_0$. In the first case, $\Phi_P/\Phi_g \ll 1$ because $\varepsilon \approx 0.099$ for helium gas and $\varepsilon \approx 0.24$ for nitrogen. On the other hand, the ratio Φ_P/Φ_g can be considerable at $R \gg R_m$. Thus, the rate is limited by the maximum value $R_m = 2R_0/\varepsilon^2$, when $\Phi_P(R)/\Phi_g \approx 1$. Therefore, substituting for $R_0 = 2\Delta T/\tau_0$ and $\tau_0 = \rho_0 c_0 d_0 L/\lambda_g$, we have for the maximum rate $R_m = 2\Delta T/\tau_m$, where the characteristic time constant equals

$$\tau_m = \frac{\rho_0 c_0 \lambda_0 d_0^2}{8\lambda_g^2}. \qquad (9)$$

Thus, τ_m equals 3.9×10^{-5} s and 1.3×10^{-3} s, as well as R_m is equal to 2.6×10^7 and 7.5×10^5 K/s, for helium and nitrogen gas, respectively. The maximum rate R_m can be further enlarged by reducing the membrane thickness.

Thus, at $R \ll R_m$ the main heat transfer from the heater is related to the heat flow through the gas $\Phi_g = (T - T_t)G$ in the direction perpendicular to the membrane. The maximal cooling rate for the empty gauge equals $(T - T_t)G/C_A$. Then, for the gauges XEN-3935 and XEN-3940 with C_0 about 20 nJ/K the maximum rate is about 10^6 K/s in helium gas at $(T - T_t) \approx 500$ K. The maximum rate is even larger – few millions K/s – for the empty gauge XEN-3973. The experiments described below were performed with the intermediate gauge XEN-3940.

2.2. *Experimental details and calorimeter performance at ultrafast rates*

The benefit of the membrane gauges with small central heated region is that the heater can be considered as a point source of a heat-flow in the gas. The heat-flow is proportional to the gas thermal conductivity, which is known in a broad temperature range down to low temperatures. This was utilized for the thermopile sensitivity calibration in a broad temperature range 5–300 K using the data for the temperature dependence of the helium gas thermal conductivity [30]. The calibration was proved by heat capacity measurements of a silver reference sample in the range 5–300 K [30]. Next, we extended the calibration up to 430 K using the data for magnetic phase transitions in $FeCr_2S_4$ at 167 K [31], Cr at 311 K [32], and melting point of indium at 429.8 K [27]. Then, the calibration was extrapolated to higher temperatures. The validity of temperature calibration for polymer samples of few microns thickness for different scanning rates was verified by measuring the glass transition temperature in different polymers as function of scanning rate.

Thus, heat capacity of a sample fixed on top of the heater (see Fig. 1) can be measured as follows. The resistive film-heater provides the heat flow $\Phi_0(t)$, which is supplied to the membrane/sample interface and transferred into the ambient gas. Generally, an appropriate lubricant can be utilized for good thermal contact between sample and membrane. The thermal contact is important for calorimetric measurements [33,34]. In case of polymers no lubricant is needed because of strong adhesive forces acting between a polymer and the membrane after first melting. Usually such contact is good and very stable. The time dependence of the temperature $T(t)$ measured at the membrane/sample interface is described by the following heat balance equation:

$$(C + C_A)\frac{dT}{dt} = \Phi_0(t) - (T - T_t)G, \tag{10}$$

This relation is correct provided the thermal thickness of the sample is small enough, that is the rate dT/dt does not exceed the acceptable maximum discussed in the previous section. The dependence $C_A(T)$ is determined from the measurements for the empty cell. Then, there are two unknown parameters $G(T)$ and $C(T)$ in Eq. (10). The heat transfer parameter $G(T)$ can be calibrated in advance [30]. Furthermore, $G(T)$ can be measured simultaneously with the sample heat capacity $C(T)$ from a heating–cooling scan as described in [19]. In order to determine the specific heat capacity, $c = C/m$, the sample mass m has to be known. This mass was not measured independently, because it was too small. It was determined from the measured heat capacity and known $c_p(T)$ in the molten state [35].

To verify the calorimeter performance at high scanning rates a second-order magnetic phase transition in a reference sample $FeCr_2S_4$ was investigated at different rates. Generally, the second-order magnetic phase transitions – such as the transition between para- and ferrimagnetic phases in $FeCr_2S_4$ – occur without any latent heat, hysteresis, and in time scale of the order of the spin relaxation time $\sim 10^{-8}$ s or even faster. Near the transition temperature the heat capacity anomaly measured at fast rate can be smeared due to the critical slowing-down of the order-parameter relaxation, but the general shape of the step-like anomaly should be independent of the rate and it should be the same at heating and cooling in a relatively broad range of scanning rates.

A plate-like single-crystalline sample about 150 ng ($\sim 45\,\mu m \times 45\,\mu m \times 20\,\mu m$ size) was placed on top of the heater of the gauge XEN-3940. About 1 μm layer of Apiezon^{TM}-N grease [36] was utilized as lubricant for good thermal contact between the sample and the membrane. First the temperature dependence of heat capacity step-like discontinuity $\Delta C(T)$ near the phase transition in $FeCr_2S_4$ was measured at slow rate 1 K/min by temperature-modulation technique (see Fig. 5). The measurements were performed at modulation frequency 80 Hz, power 10 μW, and temperature-modulation amplitude below 0.1 K. After the first scan the dependence $\Delta C(T)$ was reproducible and the same at heating and cooling. The transition temperature equals 167.7 ± 0.5 K in agreement with [31].

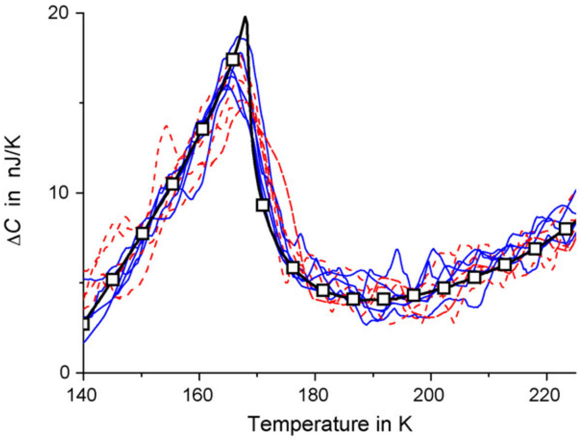

Fig. 5. Temperature dependence of the heat capacity discontinuity $\Delta C(T)$ near paramagnetic–ferrimagnetic phase transition in $FeCr_2S_4$ single-crystalline sample ca. 150 ng measured with the gauge XEN-3940 on cooling (solid lines) and heating (dashed lines) at the rates 3×10^2 K/s, 5×10^2 K/s, 10^3 K/s, 2×10^3 K/s, 3×10^3 K/s, and 10^4 K/s. The dependence $\Delta C(T)$ measured by the temperature-modulation technique for the same sample in the same gauge at slow rate 1 K/min (bold solid line marked by squares).

Then, the fast scanning experiments were performed at rates R in the range 3×10^2 to 10^4 K/s. The rate uncertainty within ±5% was caused by the change of the sample heat capacity with temperature. As shown in Fig. 5 the dependence $\Delta C(T)$ obtained at fast scanning measurements coincides with that from the temperature-modulation technique. No significant shift or $\Delta C(T)$ smearing was observed. The curves are the same at cooling and at heating as expected for the second-order magnetic phase transition. This means the apparatus and sample thermal lag is negligibly small.

Next, the method was applied for heat capacity measurements in linear polymers such as high-density polyethylene (HDPE) – standard reference material (SRM) sample – NBS SRM 1484, as well as in the samples received from Scientific Polymer Products Inc. We investigated the samples of iPS, PBT, PET, and iPP with the reference Catalog numbers 589, 961, 138, and 130, respectively. Sample mass was in the range 1–10 mg for the DSC measurements. In the case of ultrafast experiments sample mass was in the range 17–170 ng and sample thickness in the range 3–15 μm, which was determined by optical microscope Olympus$^{\mathrm{TM}}$ BX41M.

In order to verify the rate independence of temperature calibration also for polymers the glass transition temperature T_g at different rates in iPS, PET, and iPP was measured. The dependencies $T_g(R)$ were compared with the analogous curves obtained at slow rates by means of standard DSC. The results are presented at Fig. 6. The points $T_g(R)$ for DSC and fast scanning measurements lie on the same curve $\log(R) = A + B/(T_g - T_\infty) + \log(Y)$, which correspond to Vogel–Fulcher–Tamman–Hesse (VFTH) dependence $\log(\omega) = A + B/(T_g - T_\infty)$ shifted by $\log(Y) = 1.5$ [37]. The results for fast scanning measurements correspond to that of DSC as shown in Fig. 6.

Next, the temperature resolution of the ultrafast technique was tested in order to show that smearing due to thermal lag inside the sample is not essential even for rates of 10^5 K/s and low thermal conducting polymeric samples. As demonstrated previously the multiple melting peaks seen in many semicrystalline polymers at low rates are due to melting recrystallization processes [9,10,38–40]. In order to check if separate peaks can be resolved in the fast scanning experiments samples with different populations of crystals with different melting temperatures must be produced. To prepare polymer samples with two populations of crystals the molten polymer was quenched from the melt to a first and then to a second annealing temperature as shown in Fig. 7. Then, two separate melting peaks were observed at heating at 3.6×10^3 K/s as shown in Fig. 8. The higher the crystallization (annealing) temperature T_c, the larger the size of the crystals generated and the higher the melting temperature if recrystallization is avoided. Fig. 8 illustrates that the melting

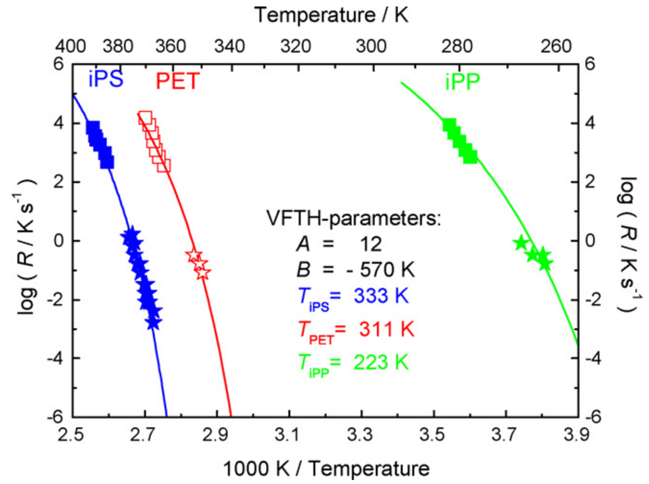

Fig. 6. Activation diagrams for iPS, PET, and iPP measured by fast scanning calorimetry (squares) and DSC (stars). The diagrams correspond to VFTH-curves (solid lines) at $A = 12$, $B = -570$ K, and $T_\infty = 333$ K, 311 K, 223 K for iPS, PET, iPP, respectively.

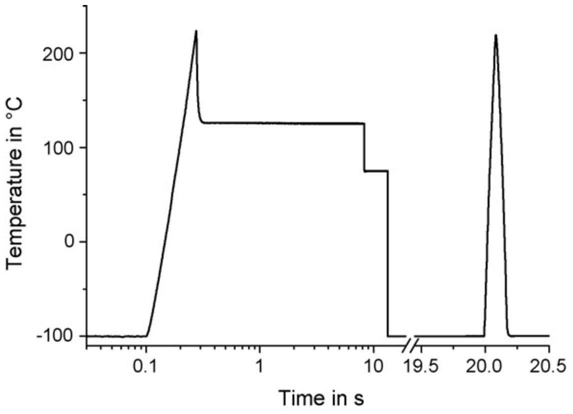

Fig. 7. Time dependence of the temperature $T(t)$ of 45 ng iPP sample during two-steps thermal processing. The sample was molted during heating from −100 °C to 220 °C at the rate 2×10^3 K/s. Then, it was quenched to 125 °C for 8 s annealing. Next, the sample was quenched to 75 °C (or 90 °C) for 5 s annealing and finally quenched to −100 °C below glass transition. The quenching rate was 10^4 K/s. After processing a heating–cooling cycle was performed to measure the multiple melting at 3.6×10^3 K/s.

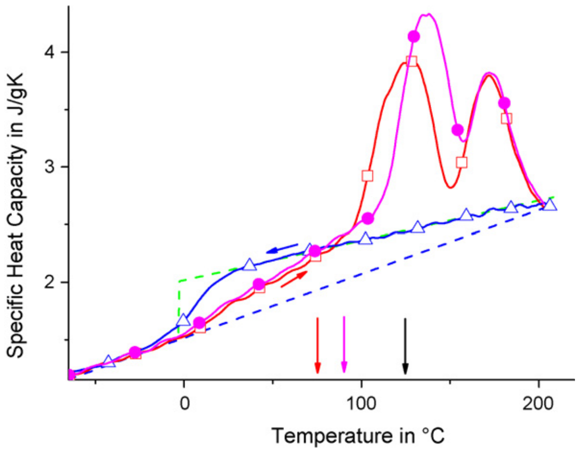

Fig. 8. Temperature dependence $c_p(T)$ of 45 ng iPP sample in the melting region at heating rate 3.6×10^3 K/s after double annealing as shown in Fig. 7. The sample was melt crystallized isothermally during 8 s at 125 °C, then annealed 5 s at 75 °C or at 90 °C (lines marked by squares and circles, respectively). The crystallization temperatures 75 °C, 90 °C, and 125 °C are indicated on the graph by arrows. The cooling curve for amorphous sample is marked by triangular. Dashed lines correspond to completely amorphous and crystalline material according to [35].

maxima related to crystalline fractions generated at two temperatures 35 K apart are well separated at ultrafast heating. The peak smearing due to the fast scanning was insignificant because the sample mass (thickness) was sufficiently small.

Next, consider HDPE, which is an extremely fast crystallizing polymer. As shown in Fig. 9 HDPE crystallizes even at quenching with the rate 1.7×10^5 K/s. We were not able to obtain amorphous polyethylene even at the rates about 0.5 MK/s. We have found for polyethylene the melting onset temperature could not be reasonably determined.

The nonadiabatic nanocalorimetry described above was successfully applied to study melting and crystallization of linear polyethylene [41], poly(ethylene terephthalate) (PET) [9,10], poly(butylene terephthalate) (PBT) [11], polyamide blends [38], isotactic polystyrene (iPS) [39] and polypropylene (PP) [40]. A more detailed study of superheating in these polymers except polyethylene will be reported elsewhere [42].

3. Melting and superheating in iPS and PBT

Next, the superheating phenomenon in a broad range of heating rates was investigated in iPS, PBT, PET, and iPP from the Scientific Polymer Products Inc. Here, as an example, we present data on iPS and PBT.

3.1. *Definition of the melting temperature: the effect of recrystallization*

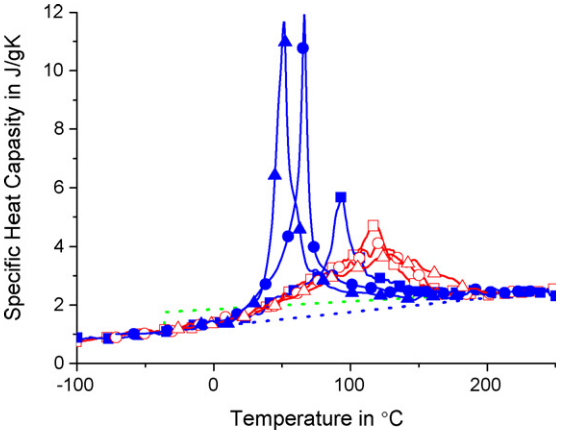

Fig. 9. Temperature dependence $c_p(T)$ of 17 ng HDPE sample at cooling from the molten state and the subsequent heating. The curves are marked by filed and open symbols correspondingly. The measurements were performed at the rates 4×10^3 K/s, 8×10^4 K/s, and 1.7×10^5 K/s (squares, circles, and triangular, respectively).

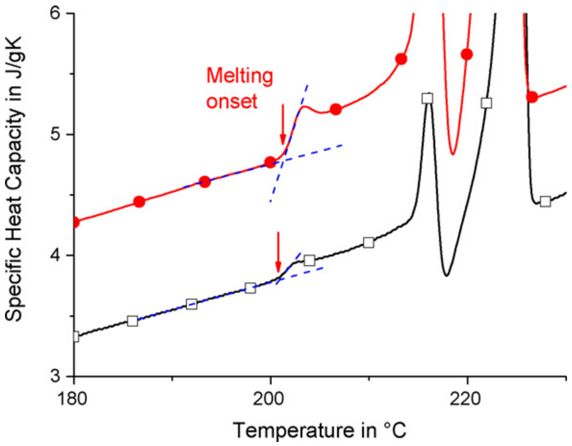

Fig. 10. Temperature dependence of the specific heat capacity $c_p(T)$ of PBT sample in the melting region at 2 K/min and 5 K/min (vertically shifted) (lines are marked by squares and circles, respectively). The sample was melt crystallized isothermally during 15 min at $T_c = 200\,°C$.

To measure the superheating in polymers the melting temperature $T_m(R)$ should be determined correctly. It is not trivial in the presence of recrystallization and remelting. Generally, the position of the maximum of the melting curve cannot be used for T_m measurements in polymers, because the melting process is accompanied by recrystallization and remelting. Thus, the shape of melting curves can be very complicated. To illustrate the problem consider the melting curves for PBT and iPS samples at relatively slow rates measured by standard DSC shown in Figs. 10 and 11. It is not obvious from the curves shown in Fig. 10 what maximum can be utilized for definition of the melting temperature T_m. The multi-peak structure of the melting curves strongly depends on the heating rate [9,10,39] and is related to recrystallization during melting. This recrystallization can be avoided at fast heating. Then, at sufficiently high rates a single melting peak can be observed [9,10,39] as in Fig. 12.

The recrystallization is initiated just after the start of melting. Then, for correct – recrystallization independent – definition of T_m it is reasonable to use just the melting onset. Although the melting onset can be strongly smeared, it is the only way to define T_m unambiguously in the presence of a recrystallization–remelting process. Another reason for using such a definition is that a possible apparatus thermal lag can cause broadening of the melting peak. Then, the maximum of the melting curve can be shifted to higher temperatures. This shift increases with increasing sample mass and the specific enthalpy of fusion related to the melting transition. On the other hand, the position of the melting onset is basically independent of such

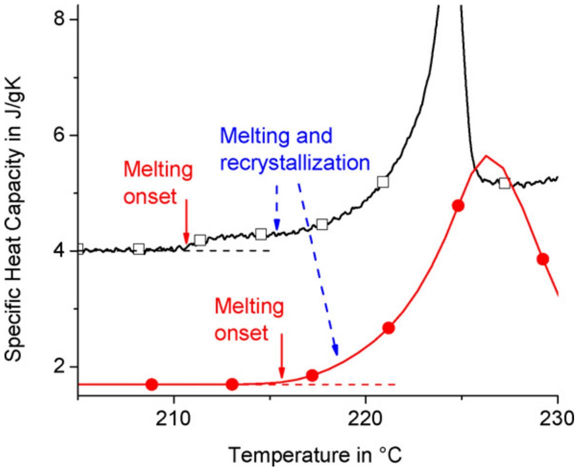

Fig. 11. Temperature dependence $c_p(T)$ of iPS in the melting region at 1 K/min (vertically shifted up) and 50 K/min (lines are marked by squares and circles, respectively). The sample was melt crystallized during 16 h at 205 °C.

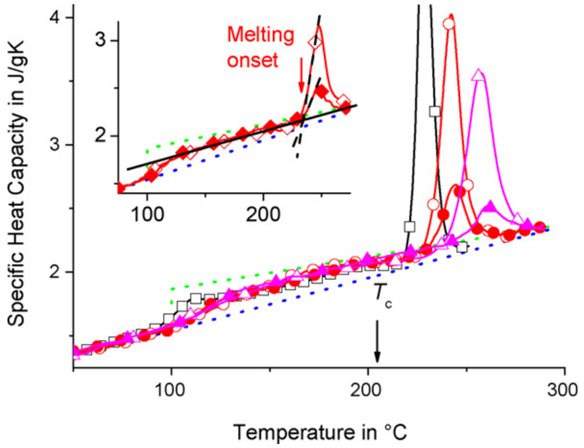

Fig. 12. Temperature dependence $c_p(T)$ of iPS in the melting region measured at 1.7 K/s (DSC), 4×10^2 K/s, and 3×10^3 K/s (lines are marked by squares, circles, and triangular, respectively). The sample was melt crystallized at 205 °C during 16 h (open symbols) and 1 h (filled symbols). Dotted lines correspond to completely amorphous and crystalline material according to [35]. Detection of the melting onset at 8×10^2 K/s is shown in the insert.

lag. Therefore, the maximum of the melting curve cannot be exploited for correct definition of the superheating rate dependence. On the other hand, the melting onset can be determined as the intersection of the extrapolated heat capacity curve before melting and the linear fit to the rising flank of the first melting peak as illustrated in Figs. 10 and 12. This way an extrapolated melting onset can be determined with reproducibility ±1 K.

3.2. Superheating measurements

First we consider the very slowly crystallizing polymer iPS. Crystallization and recrystallization in this polymer can be avoided at moderate rates. This material is suitable for DSC measurements of superheating. Figs. 11 and 12 illustrate the measurements of melting onset by DSC and the fast scanning calorimeter. As shown in Fig. 11 the effect of recrystallization is still appreciable at low rates. However the melting onset can be detected at least within the error ±1 K. The shift of T_m with the rate R is an order of magnitude higher than the uncertainty.

At fast scanning measurements the effect of recrystallization was negligible as shown in Fig. 12.

The following increment $\Delta T(R) = (T_m - T_c)$ can be used as a measure of superheating. As shown in Fig. 13 the dependence $\Delta T(R)$ obeys the power law $\Delta T(\check{R}) = A\check{R}^{\beta}$, where the dimensionless rate $\check{R}$ equals $R/(1\,\text{K/s})$, then the parameter A is in K. The equation $\Delta T(\check{R}) = A\check{R}^{\beta}$ corresponds to a straight line in the log–log plots in Fig. 13. This relation is correct in a broad range of the scanning rates. The samples of different mass 150 ng and 40 ng of iPS, as well as 170 ng and 32 ng of PBT, were measured to check the effect of apparatus thermal lag on the measured ΔT. The apparatus thermal lag should increase with the sample mass. We have found such lag to be insignificant at least for $m < 200$ ng. On the other hand, the superheating for iPS was 4 times higher than that of PBT at the same sample mass. Furthermore, for the small, 32 ng, PBT sample the measured $\Delta T(R)$ was even little bit higher than for the sample 170 ng. This is just opposite to the apparatus thermal lag and may be related to the effect of surface, which becomes noticeable with decreasing sample thickness. The most important was the effect of the sample mass on the maximum possible scanning rate, which is discussed in Section 2.1. By decreasing the sample mass we were able to achieve higher rates as shown in Fig. 13.

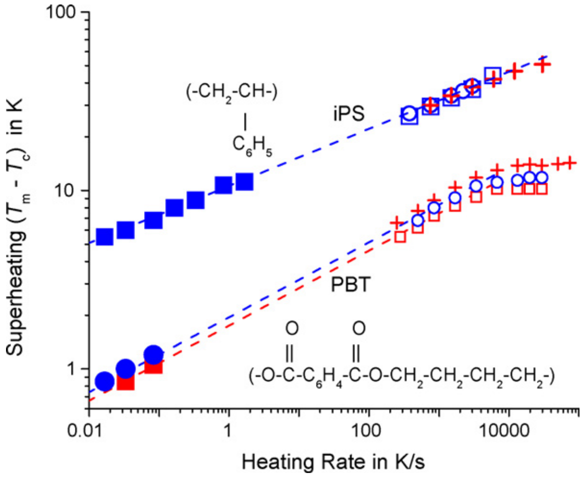

Fig. 13. Rate dependence of superheating $\Delta T = (T_m - T_c)$ measured by DSC (filled symbols), as well as by fast-scanning calorimeter in 150 ng iPS sample and 170 ng PBT sample (open symbols). The same for 40 ng iPS sample and 32 ng PBT sample (crosses). iPS samples were melt crystallized at 205 °C during 16 h (squares) and 1 h (circles and crosses), as well as PBT 15 min at 200 °C (circles), and 180 °C (squares and crosses). Dashed lines correspond to the power law $\Delta T(\check{R}) = A\check{R}^{\beta}$ at $A = 10.6$ K and $\beta = 0.16$ for iPS, as well as for PBT $\beta = 0.21$, $A = 1.95$ K and 1.75 K at $T_c = 200$ °C and 180 °C, respectively.

At high heating rates the dependence $\Delta T(R)$ tends to saturation. Such behavior is just opposite to that expected due to apparatus thermal lag and will be discussed below. At least this is an intrinsic property of the polymer, because for the same sample at the same gauge the saturation of the curve $\Delta T(R)$ can be changed by changing the annealing conditions as shown elsewhere [42].

4. Discussion and conclusions

The controlled ultrafast cooling, as well as the heating, is possible up to 10^6 K/s, with the chips available from Xensor Integration [21]. The problem of the choice of the best cooling medium for the ultrafast calorimetry is solved. It should be a gas even at a reduced pressure. Therefore, the membrane calorimetry is the optimal set up for the controlled ultrafast cooling. The dynamic model for the membrane–gas system developed to describe the ultrafast heating and cooling is in good agreement with the experiment. The characteristic rate R_0 corresponding to the quasi-static limit of the temperature change in the membrane–gas system equals 10^5 K/s for different gauges in helium gas. The range of the rates related to the quasi-static scanning is about six times broader in helium gas than in nitrogen gas and it does not depend on the gauge. Below the characteristic rate R_0 the temperature distribution in the membrane is close to the quasi-static distribution. The temperature in the membrane plane exponentially decreases with the distance from the central heating region. The characteristic length $1/\xi_0$ of the exponential decay depends on the membrane and the gas thermal conductivity, as well as on the membrane thickness. This characteristic length is about two times smaller in helium gas than in nitrogen gas. Therefore, the addenda heat capacity at the rates $R < R_0$ is few times smaller in helium gas. At high rates $R \gg R_0$ the addenda heat capacity tends to its minimum value C_0, which depends only on the size of the heated region and equals 3.0 ± 0.1 nJ/K, for the gauge XEN-3973.

The heat capacity measurements can be performed at the rates beyond the quasi-static condition, but below the limit $\sim 10^7$ K/s. This limit can be increased by reducing the membrane thickness. The sample thickness also must be small enough to avoid heat transfer limitations. The benefit of the membrane gauges with small central heated region is that the heater can be considered as a point source of a heat-flow in the gas. The maximal cooling rate can be increased by decreasing of the radius of the heated region, provided the membrane and the sample thickness are thin enough. Thus, the gauge XEN-3973 can be utilized for the faster experiments than the other gauges considered above. On the other hand, only one thermocouple can be arranged within the heating region of the gauge XEN-3973. Then, the gauges with larger heating region should be used for moderate rates.

Strong superheating was observed in iPS and PBT, as well as in other linear polymers (PET and iPP not shown here). We have found, independent on the presence of a recrystallization–remelting process, the melting onset can be utilized as an appropriate definition of the melting temperature T_m. The increment $\Delta T = (T_m - T_c)$ is an appropriate definition of a superheating in the linear polymers, where T_c is the temperature of crystallization. The heating rate dependence of the superheating in the linear polymers is described by the power law of the dimensionless rate $\check{R} = R/(1\,\text{K/s})$:

$$\Delta T(\check{R}) = A\check{R}^{\beta} \tag{11}$$

The parameter A changes in the range 2–10 K for different polymers and it depends on the annealing temperature T_c. The exponent β changes in the range 0.16–0.21 for different polymers and only slightly depends on T_c. The most pronounced effect of the annealing temperature was observed for the maximum value of the superheating $\Delta T_{\max}$. The maximum value of the superheating can reach 10% of T_m as in iPS. The physical reason for the superheating limit in polymers will be discussed elsewhere [42]. The measured superheating is definitely not related to the apparatus thermal lag on the following reasons. It does not depend on the sample mass, and on the transition enthalpy (crystallinity), but it depends on the annealing conditions for the same sample in the same gauge as shown elsewhere [42]. The observed phenomenon of the spontaneous melting above the upper limit of the superheating is just opposite to the apparatus thermal lag, which must lead to the increase of the lag at high rates. No saturation of the dependence $\Delta T(R)$ can be observed in the case of apparatus lag. Apparatus thermal lag due to thermal gradients in the system can be proportional to R^{β} with $\beta \sim 1$. On the contrary, the observed superheating depends on the rate as R^{β} with $\beta \sim 0.1$.

The Eq. (11) is satisfied in a broad range of the heating rates. This dependence is a straight line in the double logarithmic plot at least on the scale of 6 orders of magnitude (Fig. 13). Thus, we have the evidence that $\lim_{R\to 0} T_m(R)$ is equal to T_c at least within accuracy ± 1 K. This result is not surprising for the semicrystalline materials, in which heterogeneous melting can take place at the interface between the amorphous and the crystalline phases. Therefore, the melting can start at a temperature just above T_c. Nevertheless, the melting process can be slowed down due to an energy barrier retarding the crystalline–amorphous interface movement. Then, the polymer can be superheated significantly above T_c at sufficiently fast heating. Noteworthy, the result $\lim_{R\to 0} T_m(R) = T_c$ is important for the better understanding of the crystallization process in the linear polymers.

Acknowledgement

The financial support of the German Science Foundation (DFG), grant number 436 RUS 17/117/05 and Senter/Novem, The Netherlands, project IS041029, are gratefully acknowledged.

References

[1] G. Strobl, Prog. Polym. Sci. 31 (2006) 398.
[2] J.G. Dash, Rev. Mod. Phys. 71 (1999) 1737.
[3] J.G. Dash, Contemp. Phys. 43 (2002) 427.
[4] E. Hellmuth, B. Wunderlich, J. Appl. Phys. 36 (1965) 3039.
[5] J. Clements, I.M. Ward, Polymer 23 (1982) 935.
[6] J.E.K. Schawe, G.R. Strobl, Polymer 39 (1998) 3745.
[7] K. Yamada, M. Hikosaka, A. Toda, S. Yamazaki, K. Tagashira, Macromolecules 36 (2003) 4790.
[8] A. Toda, M. Hikosaka, K. Yamada, Polymer 43 (2002) 1667.
[9] A.A. Minakov, D.A. Mordvintsev, C. Schick, Polymer 45 (2004) 3755.
[10] A.A. Minakov, D.A. Mordvintsev, C. Schick, Faraday Discuss. 128 (2005) 261.
[11] M. Pyda, E. Nowak-Pyda, J. Heeg, H. Huth, A.A. Minakov, M.L. Di Lorenzo, C. Schick, B. Wunderlich, J. Polym. Sci. B: Polym. Phys. 44 (2006) 1364.
[12] A.B. Belonoshko, N.V. Skorodumova, A. Rosengren, B. Johansson, Phys. Rev. B 73 (2006) 012201.
[13] X.-M. Bai, M. Li, Phys. Rev. B 72 (2005) 052108.
[14] H.J. Fecht, W.L. Johnson, Nature 334 (1988) 50.
[15] J.L. Tallon, Nature 342 (1989) 658.
[16] M. Born, J. Chem. Phys. 7 (1939) 591.
[17] F.A. Lindemann, Z. Phys. 11 (1910) 609.
[18] K. Lu, Y. Li, Phys. Rev. Lett. 80 (1998) 4474.
[19] A.A. Minakov, S.A. Adamovsky, C. Schick, Thermochim. Acta 432 (2005) 177.
[20] A.A. Minakov, J. Morikawa, T. Hashimoto, H. Huth, C. Schick, Meas. Sci. Technol. 17 (2006) 199.
[21] A.W. van Herwaarden, Thermochim. Acta 432 (2005) 192, Technical data available on the website: http://www.xensor.nl/.
[22] S.L. Lai, G. Ramanath, L.H. Allen, P. Infante, Z. Ma, Appl. Phys. Lett. 67 (1995) 1229.
[23] E.A. Olson, M.Y. Efremov, M. Zhang, Z. Zhang, L.H. Allen, J. Micromech. Syst. 12 (2003) 3.
[24] S.L. Lai, J.Y. Guo, V. Petrova, G. Ramanath, L.H. Allen, Phys. Rev. Lett. 77 (1996) 99.
[25] M.Y. Efremov, F. Schiettekatte, M. Zhang, E.A. Olson, A.T. Kwan, R.S. Berry, L.H. Allen, Phys. Rev. Lett. 85 (2000) 3560.

[26] M.Y. Efremov, E.A. Olson, M. Zhang, S.L. Lai, F. Schiettekatte, Z. Zhang, L.H. Allen, Thermochim. Acta 412 (2004) 13.
[27] D.R. Lide, Handbook on Chemistry and Physics, 79th ed., CRC Press, 1998–1999 (Chapters 4, 6, 12).
[28] P.M. Sarro, A.W. van Herwaarden, M. Iodice, Thermophysical properties of low stress poly- and mono-silicon and silicon-nitride, in: Proceedings of Eurosensors VIII, Toulouse, France, 1994.
[29] B. Revaz, B.L. Zink, D. O'Neil, L. Hull, F. Hellman, Rev. Sci. Instrum. 74 (2003) 4389.
[30] A.A. Minakov, S.B. Roy, Y.V. Bugoslavsky, L.F. Cohen, Rev. Scien. Instr. 76 (2005), art. no. 043906.
[31] V. Fritsch, J. Deisenhofer, R. Fichtl, J. Hemberger, H.-A. Krug von Nidda, M. Mucksch, M. Nicklas, D. Samusi, J.D. Thompson, R. Tidecks, V. Tsurcan, A. Loidl, Phys. Rev. B 67 (2003) 144419.
[32] E. Fawcett, Rev. Mod. Phys. 60 (1988) 209.
[33] I. Hatta, A.A. Minakov, Thermochim. Acta 330 (1999) 39.
[34] A.A. Minakov, Thermochim. Acta 345 (2000) 3.
[35] B. Wunderlich, Pure Appl. Chem. 67 (1995) 1019, http://athas.prz.edu.pl/databank/welcome-db.html.
[36] Technical data available on the website: http://www.2spi.com/catalog/vac/apiezon-ncryo.html.
[37] A. Hensel, C. Schick, J. Non-Cryst. Sol. 235 (1998) 510.
[38] R.T. Tol, A.A. Minakov, S.A. Adamovsky, V.B.F. Mathot, C. Schick, Polymer 47 (2006) 2172.
[39] A.A. Minakov, D.A. Mordvintsev, R.T. Tol, C. Schick, Thermochim. Acta 442 (2006) 25.
[40] A. Gradys, P. Sajkiewicz, A.A. Minakov, S.A. Adamovsky, C. Schick, T. Hashimoto, K. Saijo, Mater. Sci. Eng. A: Struct. Mater. Prop. Microstruct. Process. 413 (2005) 442.
[41] S.A. Adamovsky, A.A. Minakov, C. Schick, Thermochim. Acta 403 (2003) 55.
[42] A.A. Minakov, A. Wurm, C. Schick, Eur. Phys. J. E, Submitted for publication.